https://doi.org/10.3311/PPci.39878

Periodica Polytechnica Civil Engineering, 69(3), pp. 850–868, 2025

Volume of Fluid Implementation of Water Inrush and Escape Route Optimization in Tunnel

Dongdong Pan[1,2], Shuo Tai[1], Weijia Xu[1], Yuchao Du[3*], Hongbin Chen[4], Andong Hu[1]

[1] School of Qilu Transportation, Shandong University, East Second Ring Road 12550, 250002 Jinan, China
[2] State Key Laboratory of GeoMechanics and Deep Underground Engineering, China University of Mining and Technology, University Road 1, 221116 Xuzhou, China
[3] School of Civil Engineering, Shandong University, Jingshi Road 17923, 250061 Jinan, China
[4] Graduate School of Engineering, Nagasaki University, Bunkyo 1-14, 852-8521 Nagasaki, Japan
[*] Corresponding author, e-mail: ycdu@sdu.edu.cn

Received: 15 January 2025, Accepted: 10 April 2025, Published online: 27 May 2025

Abstract

Water inrush is the most common tunnel engineering disaster, which seriously threatens the life safety of construction personnel. Effective escape route planning is an important measure to reduce casualties. The effects of water inrush velocity, water inlet diameter, water inrush inlet position and water outlet condition on the tunnel water inrush are analyzed by numerical simulation based on VOF (volume of fluid). The results reveal that the tunnel with the water inrush side is the dominant channel of water inflow, and its water level and flow velocity are greater than that of the cross passage, which is the priority escape channel. After water flows to the tunnel port and rushes back, the water level in the tunnel increases rapidly, forming an obvious flow velocity and water level sudden change front. Increasing the water inrush velocity or the water inlet diameter, the increase of the water flowrate makes the water level and flow velocity in the tunnel larger. Water inflow from baseplate is more likely to form high water level and high flow velocity. Escape route recommendations: From the inside wall of the tunnel with water inrush side, through the inside wall of the cross passage to the tunnel without water inrush side to take refuge, and finally through the inside wall of the tunnel to escape from the tunnel with water inrush disaster. This study has certain guiding significance for the escape route design of tunnel water inrush engineering disasters.

Keywords

tunnel water inrush, numerical simulation, flow characteristics, escape route

1 Introduction

With the rapid development of China's economic construction, the construction of tunnel engineering presents a long, large and deep development trend. Karst and unfavorable geology problems induce frequent water and mud inrush geological disasters in the process of tunnel construction, resulting in serious casualties, economic losses, environmental damage and construction delay [1, 2]. For example: Longshan-Yongshun Highway dam tunnel in the excavation process exposes a number of large karst caves, and large-scale water inrush disasters occurred many times, with the maximum water inflow up to 1.4 × 10^4 m^3/h [3]. During the construction of Maluqing tunnel of Yichang-Wanzhou Railway, the surrounding rock of the arch is fractured by the overlying cavity water, and the water inrush disaster occurs, and the maximum water inrush is up to 30 × 10^4 m^3/h [2]. The maximum water inflow of DK124 + 602 high-pressure water-rich cavity in Yesanguan Tunnel of Yichang-Wanzhou Railway is 2 × 10^4 m^3/h [4]. Xiushan Tunnel of Yuxi-Mengzi Railway is rich in groundwater, mainly karst pipeline water and bedrock fissure water, and the maximum water inflow is 9.8 × 10^3 m^3/h [5]. The geological disaster of water and mud inrush has become a bottleneck problem restricting the development of tunnel construction and an urgent engineering problem to be solved in China. The photos of water inrush in the tunnel are shown in Fig. 1 [3, 6, 7].

At present, domestic and foreign scholars have done a lot of research on the prevention and control of water and mud inrush geological disasters in tunnel engineering, such as the disaster-causing structure of water and mud inrush in tunnel [6, 8, 9], the detection and identification of unfavorable geology [10], the disaster-causing

Cite this article as: Pan, D.,Tai, S., Xu, W., Du, Y., Chen, H., Hu, A. "Volume of Fluid Implementation of Water Inrush and Escape Route Optimization in Tunnel", Periodica Polytechnica Civil Engineering, 69(3), pp. 850–868, 2025. https://doi.org/10.3311/PPci.39878

(a) (b)

(c) (d)

Fig. 1 Water inrush in tunnels [3, 6, 7]: (a) Ma luqing tunnel, (b) Jinping II station tunnel, (c) Qiyue mountain tunnel, (d) Xiangyun tunnel

mechanism of water and mud inrush [11] the prediction, early warning and prevention and control of geological disasters [12, 13], the risk assessment of water inrush in tunnel [14–16] and the grouting research of water inrush in tunnel [17–19]. In the aspect of tunnel water inrush simulation, He [20] used Flow-3D to simulate the movement mode of karst tunnel water inrush based on Baofeng tunnel project. Zhou et al. [21] established the conceptual model of mine water inrush, captured the three characteristics of mine water inrush, water inrush process and submerged process, and simulated the process of underground excavation and virtual water inrush disaster. Zhang et al. [22] proposed a space-time model based on pipe flow theory to simulate the diffusion process of water inrush in mine road network. Feng et al. [23, 24] resolved the numerical noise problem of liquid-solid coupling through a single-layer two-phase SPH model and dynamic free surface boundary algorithm, achieving high-precision simulation of the entire process of unsaturated soil seepage-deformation, and promoting the application of meshless methods in the evolution prediction of multiphase flow in hydrogeological disasters. In the optimization of tunnel escape route, Holický [25] used Bayesian networks supplemented by decision nodes and utility nodes to analyze the risk of highway tunnels and optimize escape routes; Yan and Feng [26] optimized the ant algorithm and proposed a new escape route planning method for underground mines, it is verified that this method can effectively find a good escape route and can be used for escape route planning of large and medium-sized underground coal mines. Ali et al. [27] used geographic information system (GIS) for network analysis and determined the best escape route from different underground locations to safe locations inside and outside the mine when the fire occurred.

However, existing studies on the refined simulation of dynamic flow characteristics during tunnel water inrush disasters [28, 29] and their guiding implications for escape route optimization remain significantly inadequate. Current research predominantly employs numerical methods based on pipe flow theory or simplified fluid models, which, while capable of reflecting macroscopic flow trends, exhibit limitations in capturing dynamic gas-liquid interface evolution, localized abrupt velocity fronts, and complex backflow phenomena. In contrast, this study innovatively introduces the VOF (Volume of Fluid) method to achieve refined characterization of unsteady flow, rapid water-level front formation, and secondary water inrush phenomena in connecting channels during tunnel water inrush processes, through precise tracking of free liquid surfaces and fluid volume fractions. Furthermore, this paper systematically reveals the three-stage evolution law of water level (rising, maintaining, and turbulent phases) in the water-inrush-side tunnel acting as a dominant channel, and proposes risk-avoidance path optimization strategies based on VOF simulation results. Compared to traditional methods, the VOF model not only enables quantitative analysis of flow field characteristics under coupled effects of multiple factors (e.g., inrush velocity, inlet diameter/position, and outlet conditions) but also provides scientific dynamic water-level and velocity thresholds for escape route selection. This approach not only addresses the insufficient resolution of dynamic flow field analysis in existing studies but also establishes a more universal theoretical framework for escape route design in tunnel water inrush disasters under complex geological conditions.

2 Numerical simulation method of water inrush

2.1 Control equation

The following assumptions are made for the tunnel water inrush model:

1. There is a two-phase flow in the tunnel, and the water and air are incompressible homogeneous isotropic fluids.
2. When the gushing water flows in the tunnel, the wall surface is non-slip condition.
3. The tunnel wall is impermeable, that is, the gushing water does not seep out of the tunnel wall.
4. Water and air viscosity do not change with time.
5. The water flow is affected by gravity, and the gravity acceleration is 9.8 m^2/s, without considering the surface tension.
6. Ignore the influence of construction equipment in the tunnel on the flow field.

The control equation of water inrush disaster development process includes:

1. The continuity equation is:

$$\frac{\partial \rho}{\partial t} + \nabla \cdot \left(\rho \boldsymbol{U} \right) = 0 . \tag{1}$$

2. And the momentum equation is:

$$\frac{\partial \rho \boldsymbol{U}}{\partial t} + \nabla \cdot \left(\rho \boldsymbol{U} \otimes \boldsymbol{U} \right) - \nabla \cdot \tau = -\nabla p + \rho \boldsymbol{g} . \tag{2}$$

Where ρ is the density, $\boldsymbol{U}$ is the velocity, p is the pressure, τ is the effective stress, and $\boldsymbol{g}$ is the gravity acceleration.

In order to obtain the diffusion range of tunnel gushing water, the VOF (volume of fluid) model is used to solve the two-phase interface problem. In the VOF method, a variable α is defined to represent the phase fraction of the fluid. Considering the gas-liquid two-phase system of a grid cell, if the grid cell is filled with fluid, then $\alpha = 1$; if the grid cell is filled with gas, then $\alpha = 0$; if the value of α is between 0 and 1, the gas-liquid mixture is present in this grid cell.

By solving and converting, the momentum equation of VOF model can be obtained:

$$\begin{aligned} &\frac{\partial \rho \boldsymbol{U}}{\partial t} + \nabla \cdot \left(\rho \boldsymbol{U} \boldsymbol{U} \right) - \nabla \cdot \left(v \nabla \boldsymbol{U} \right) - \nabla \boldsymbol{U} \cdot \nabla v \\ &= -\nabla p_{rgh} - \boldsymbol{g} \cdot \boldsymbol{h} \nabla \rho , \end{aligned} \tag{3}$$

where $\nabla p_{rgh} = \nabla p - \boldsymbol{g} \cdot \boldsymbol{h} \nabla \rho - \rho \boldsymbol{g}$.

Then the phase equation in the VOF model is derived:

$$\frac{D\rho}{Dt} = \frac{D\left(\alpha \left(\rho_1 - \rho_2 \right) + \rho_2 \right)}{Dt} = \frac{D\alpha}{Dt} = \frac{\partial \alpha}{\partial t} + \boldsymbol{U} \cdot \nabla \alpha = 0 . \tag{4}$$

Where ρ_1 and ρ_2 denote the densities of the two fluids respectively.

2.2 Numerical discretization method

In order to construct a discrete matrix about velocity and pressure, the finite volume discretization of Eq. (3) is carried out and organized as a matrix about the velocity of the control volume center:

$$A_P \boldsymbol{U}_P^r + \sum A_N \boldsymbol{U}_N^r = S_P^n . \tag{5}$$

Where $\boldsymbol{U}_P^r$ and $\boldsymbol{U}_N^r$ are the predicted velocity of the present and neighboring control volume centers, the superscript r denotes the residual term at the current iteration step, A_P and A_N are the matrix coefficient, and the remaining known quantities unrelated to the velocity of the control volume center enter the right side S_P of the equation where S_P is the linearization coefficient of the source term, and the superscript n represents the current time step. According to the continuity equation, considering the final convergence, the Eq. (1) is discretized to obtain:

$$\sum\left(\boldsymbol{U}_{P,f}^{n+1}\cdot\boldsymbol{S}_f\right)=0\,. \tag{6}$$

Where the subscript f represents the value on the surface of the grid unit, $\boldsymbol{S}_f$ represents the surface vector of each surface of the grid unit. If the pressure can be expressed $\boldsymbol{U}_{P,f}^{n+1}$ in Eq. (6), the pressure Poisson equation can be constructed. In the case of convergence, Eq. (5) is expressed as follows:

$$A_P\boldsymbol{U}_P^{n+1}+\sum A_N\boldsymbol{U}_N^{n+1}=S_P^n-\nabla p_{rgh,P}-\boldsymbol{g}\cdot\boldsymbol{h}\nabla\rho_P\,. \tag{7}$$

Where the subscript rgh denotes the reconstructed pressure.

Define $\boldsymbol{HbyA}_P^{n+1}=\dfrac{1}{A_P}\left(-\sum A_N\boldsymbol{U}_N^{n+1}+S_P^n\right)$, then

$$\boldsymbol{U}_P^{n+1}=\boldsymbol{HbyA}_P^{n+1}-\frac{1}{A_P}\left(\nabla p_{rgh,P}^{n+1}+\boldsymbol{g}\cdot\boldsymbol{h}\nabla\rho_P^{n+1}\right). \tag{8}$$

Where $\boldsymbol{HbyA}$ denotes $\boldsymbol{H}$ divided by the diagonal coefficient $\boldsymbol{A}$, $\boldsymbol{H}$ is the explicit part of the momentum equation, and $\boldsymbol{A}$ is the diagonal coefficient matrix of the momentum equation.

$$\boldsymbol{U}_{P,f}^{n+1}=\boldsymbol{HbyA}_{P,f}^{n+1}-\frac{1}{A_{P,f}}\left(\left(\nabla p_{rgh,P}^{n+1}\right)_f+\boldsymbol{g}\cdot\boldsymbol{h}\left(\nabla\rho_P^{n+1}\right)_f\right) \tag{9}$$

Bring Eq. (9) into Eq. (6):

$$\begin{aligned}&\sum\left(\boldsymbol{HbyA}_{P,f}^{n+1}+\frac{1}{A_{P,f}}\left(-\boldsymbol{g}\cdot\boldsymbol{h}\left(\nabla\rho_P^{n+1}\right)_f\right)\right)\\&=\sum\frac{1}{A_{P,f}}\left(\nabla\left(p_{rgh,P}^{n+1}\right)_f\right).\end{aligned} \tag{10}$$

That is,

$$\nabla\cdot\left(\frac{1}{A}\nabla p_{rgh}^{n+1}\right)=\nabla\cdot\left(\boldsymbol{HbyA}^{n+1}+\frac{1}{A}\left(-\boldsymbol{g}\cdot\boldsymbol{h}\nabla\rho^{n+1}\right)\right). \tag{11}$$

Solving Eq. (11) has the pressure of convergence. In this paper, the pressure implicit with splitting of operators (PISO) algorithm is used to correct several times in a time step to obtain the corrected pressure-velocity coupling results.

2.3 Validation of two-phase VOF model

To validate the effectiveness of the two-phase Volume of Fluid model adopted in this study, numerical simulations were conducted based on the internationally recognized dam-break benchmark test. The numerical setup strictly followed the classical experimental parameters established by Koshizuka [30]: The computational domain was configured with dimensions of length × height = 0.584 m × 0.584 m, featuring an initial water column of height H = 0.292 m on the left side and an air domain on the right.

Fig. 2 presents a comparative analysis between the simulated water phase morphology and experimental measurements at two characteristic time instants (t = 0.2 s and t = 0.4 s) during dam-break evolution. The numerical model successfully reproduces critical hydrodynamic processes including water column collapse, leading-edge propagation, wall impact, and reflux development. Notably, the numerical results demonstrate excellent agreement with experimental data in terms of gas-liquid interface morphology and front propagation velocity.

These validation results confirm that the implemented two-phase VOF model accurately captures both mass transport characteristics and dynamic interface evolution behavior in gas-liquid systems, thereby establishing a reliable theoretical foundation for subsequent multiphase flow simulations of tunnel water inrush phenomena.

3 Tunnel water inrush simulation and result analysis

3.1 Calculation model and working condition

A three-dimensional model of 100 m tunnel behind the tunnel workface is established. The cross passage is located 48 m behind the workface and 4 m wide. As shown in Fig. 3 and Fig. 4, the tunnel radius is 5 m, the distance from the center of the tunnel to baseplate V1 is 3 m, the height of the cross passage V4 is 4 m, the length of the tunnel baseplate H3 is 8 m. H4 is 11 m, the length of the cross passage H5 is 22 m, and the distance between the central axis of the left and right tunnels is 30 m.

Four factors on the water inrush process are considered, including water inrush velocity, water inlet diameter, water inlet position and water outlet condition. The water inlet is simplified to a circle. The water inlet and water outlet are shown in Fig. 4. The water inflow velocity levels are 5 m/s, 4 m/s and 3 m/s. The water inlet diameter levels are 2 m, 1.5 m and 1 m. The working conditions are shown in Table 1.

The water flowrate in the working condition is between 8.5×10^3 m^3/h and 3.4×10^4 m^3/h. Compared with the flowrate of water inrush geological disasters in the practical projects [2–5], the water flowrate designed in the work condition accords with the engineering practice.

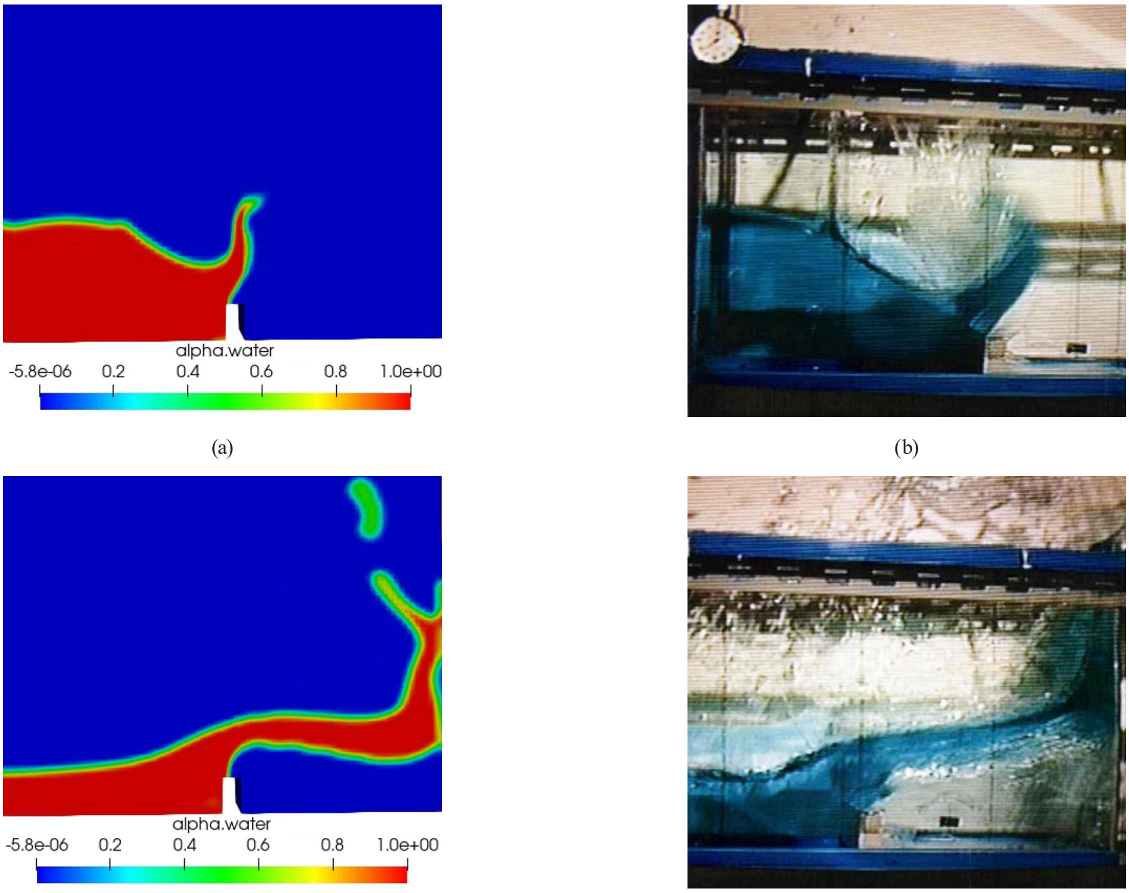

(a) (b)

(c) (d)

Fig. 2 Comparison of numerical results with dambreak experiment: (a) Numerical results (t = 0.2 s), (b) Experiment (t = 0.2 s) [30], (c) Numerical results (t = 0.4 s), (d) Experiment (t = 0.4 s) [30]

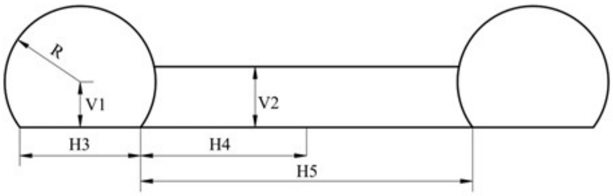

Fig. 3 Cross section size of tunnel model

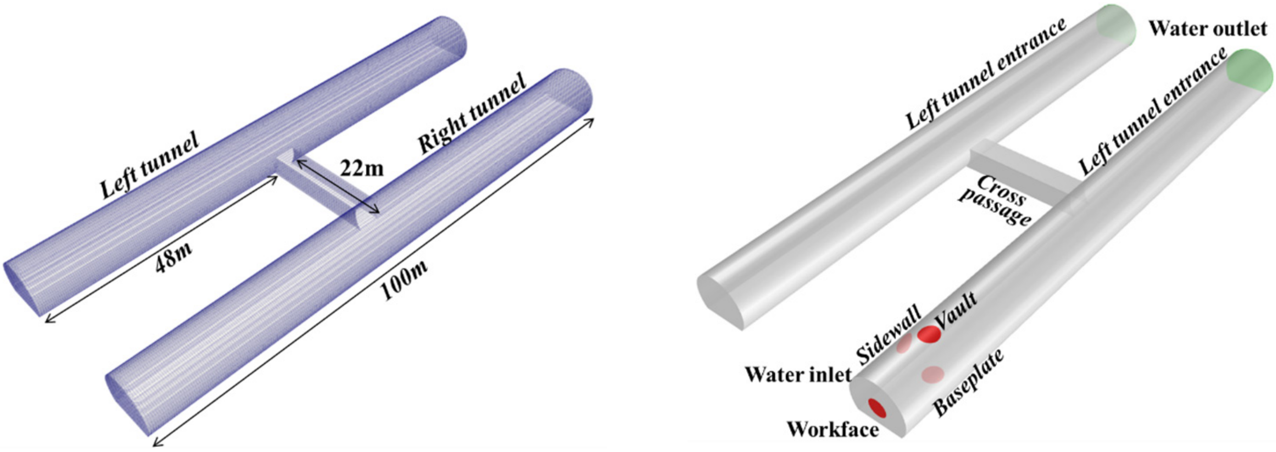

(a) (b)

Fig. 4 Tunnel model: (a) Tunnel grid division, (b) Location of water inlet and outlet

Table 1 Working condition table

Factors	Water inlet	*v* (m/s)	*D* (m)	Water outlet
Water inrush velocity	Workface $X = 15$ m, $Y = 3$ m, $Z = 0$ m	3 4 5	1	Left tunnel entrance
Water inlet diameter	Workface $X = 15$ m, $Y = 3$ m, $Z = 0$ m	3	1 1.5 2	Left tunnel entrance
Water inlet position	Sidewall $X = 10$ m, $Y = 3$ m, $Z = -10$ m Vault $X = 15$ m, $Y = 8$ m, $Z = -10$ m Baseplate $X = 15$ m, $Y = 0$ m, $Z = -10$ m	5	1	Left tunnel entrance
Water outlet condition	Workface $X = 15$ m, $Y = 3$ m, $Z = 0$ m	5	1	Left tunnel entrance Left tunnel and right tunnel entrance

3.2 Analysis of the influence of water inrush velocity on the results

The tunnel on the water inrush side is the most important area affected by water damage, so the cross sections of the right tunnel $Z = -5$ m, $Z = -25$ m, $Z = -45$ m, $Z = -65$ m, $Z = -85$ m is taken as the monitoring surfaces, as shown in Fig. 5. The water level in the tunnel is an important indicator for analyzing the water inrush process and optimizing the escape route. The ratio of water inrush distribution to alpha.water is defined as Eq. (12) to reflect the water level of the monitoring surfaces.

$$\text{alpha.water} = \frac{V_{\text{water}}}{V_{\text{water}} + V_{\text{air}}} \qquad (12)$$

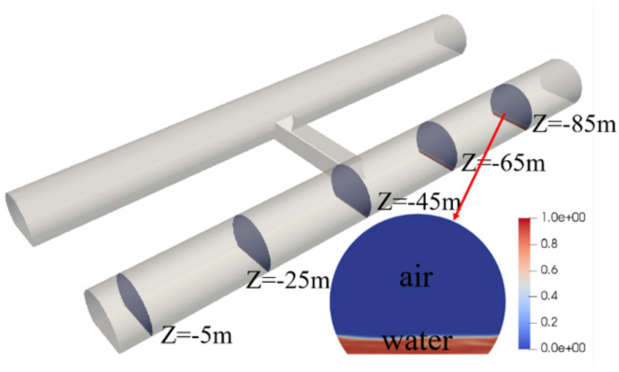

Fig. 5 Layout of monitoring surfaces

Only the water inrush velocity is changed, as shown in Table 1, and the trend of water level change on the monitoring surfaces is shown in Fig. 6.

Fig. 6 shows that the water level change of the right tunnel is divided into three stages: water level rising period

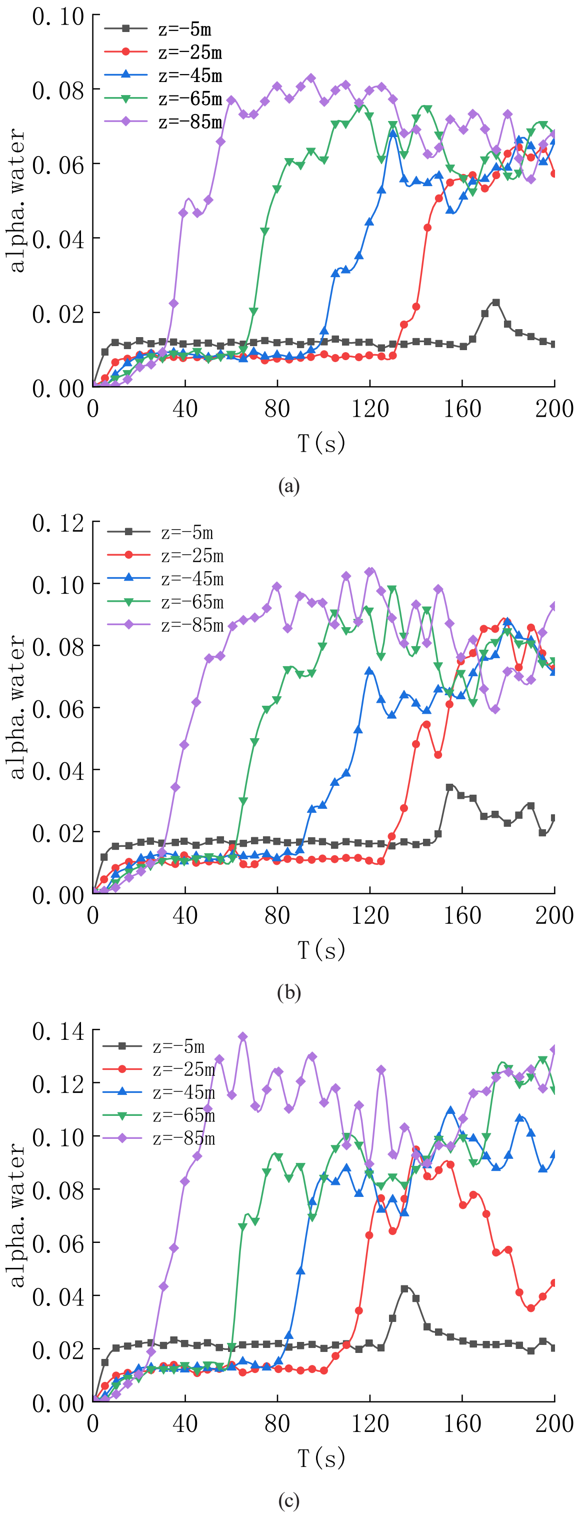

Fig. 6 Monitoring surfaces water level variation trend: (a) $v = 3$ m/s, (b) $v = 4$ m/s, (c) $v = 5$ m/s

(Period 1), water level maintaining period (Period 2), and water level disorder period (Period 3). After the water inrush occurs in the tunnel, the water level rises to a certain level, which is defined as the water level rising period. The stage when the water level is maintained at this level is defined as the water level maintaining period; the period when the water level rises rapidly and fluctuates up and down is defined as the water level disorder period. The water gushing back at the end of the right tunnel leads to the disorder of the water level in the tunnel. In addition, the water level during the water level maintaining period and the degree of water level disorder are positively correlated with the water inrush velocity. The velocity of water rushing back can be judged from the time interval from each monitoring surface to the water level disorder period, so the velocity of water rushing back increases with the increase of the water inrush velocity.

The water level variation trend at the cross-section $X = 10$ m near the intersection of the right tunnel and the cross passage is depicted in Fig. 7. Only when the water inflows into the cross passage, the water level increases rapidly. The right tunnel is the dominant channel for water inrush flow, indicating that after the water inrush disaster occurs on the tunnel workface, it should be avoided from the cross passage as soon as possible before the water rushes back.

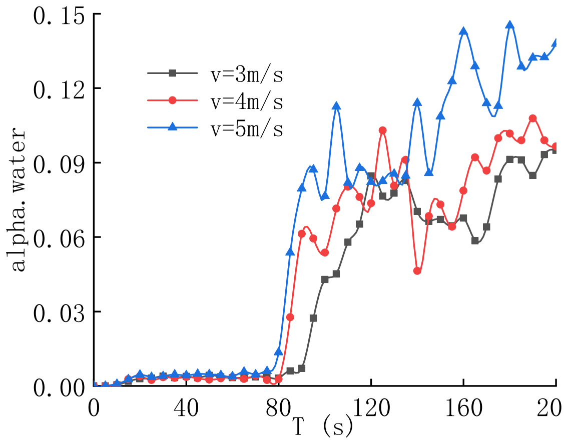

Fig. 7 Cross passage water level variation trend

During the water level disorder period, the water level fluctuates chaotically and there is no obvious rule. Therefore, the water level in the right tunnel with different water inrush velocities of $t = 20$ s is compared. The water inrush flow pattern is shown in Fig. 8, and the water level comparison is shown in Fig. 9.

Fig. 8 indicates that the water level in the cross passage is much lower than that in the right tunnel. The larger the water inrush velocity is, the higher the water accumulation level in the tunnel is, but the water level does not change significantly with the water inrush velocity. Fig. 9 shows that the closer the distance from the water gushing point is, the higher the water level in the tunnel is, and the water level at $Z = -85 \sim -100$ m increases sharply, indicating that the water gushing at the selected time has just begun to rush back.

3.3 Analysis of the influence of water inlet diameter on the results

Only the water inlet diameter is changed, as shown in Table 1. The change trend of the water level of the monitoring surfaces is shown in Fig. 10.

It can be seen from Fig. 10 that only the water inlet diameter (D) is changed, the water level change of the right tunnel is still divided into three stages: the water level rising period, the water level maintaining period and the water level disorder period. During the water level maintaining period, the water level, the degree of water level disorder and the velocity of water rushing back are positively correlated with the water inlet diameter. When $D = 2$ m, the water level in the

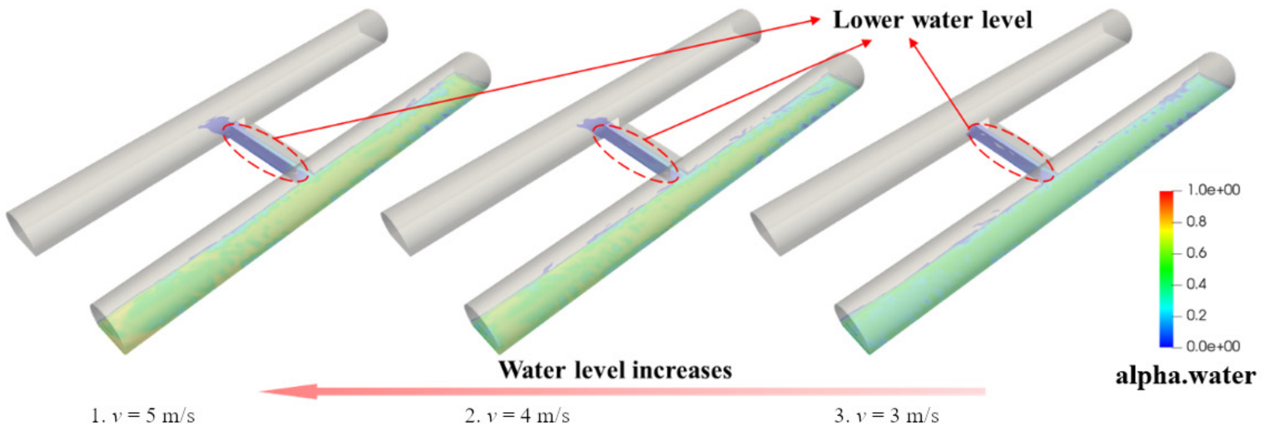

1. $v = 5$ m/s 2. $v = 4$ m/s 3. $v = 3$ m/s

Fig. 8 Water inrush flow pattern

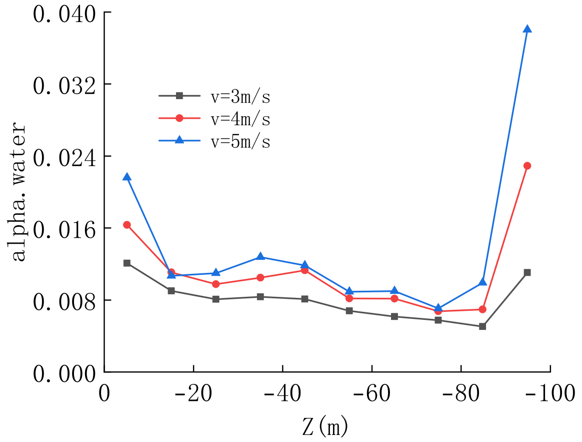

Fig. 9 Comparison of water levels in the right tunnel

tunnel has a more obvious gradient, and the water inflow potential energy is converted into kinetic energy, which makes the water inrush velocity in the tunnel larger.

The water level change trend of the cross section of the cross passage at $X = 10$ m is shown in Fig. 11. The water level at $D = 2$ m is obviously higher, and the water level of the cross passage increases rapidly after the back-inrush water enters, indicating that the right tunnel is the dominant channel for water inrush.

Comparing the water level of the right tunnel under different water inlet diameters when $t = 20$ s before the water level disorder period, the water inrush flow pattern is shown in Fig. 12, and the water level comparison is shown in Fig. 13.

Fig. 12 and Fig. 13 show the water level in the cross passage is much lower than that in the right tunnel. The shape of the water gushing into the left tunnel at this moment shows that the water gushing velocity in the tunnel is the largest when D = 2 m, and the larger the water inlet diameter is, the higher the water level in the tunnel is. The water level in the tunnel changes obviously with the water inlet diameter, and the water level at $Z = -85 \sim -100$ m increases sharply, indicating that the water inrush has just begun to rush back at the selected time. Compared with the water inrush velocity, the water inlet diameter has a greater influence on the water level in the tunnel. The water inrush velocity and the water inlet diameter directly affect the flowrate of water inrush. Equation (13) explains the water inlet diameter has a greater influence on the flowrate of water inrush (Q). The larger the flowrate of water inrush is, the higher the water level of water inrush accumulation in the tunnel is, the water inrush potential energy is converted into kinetic energy, and the water inrush velocity is faster.

$$Q = \frac{\pi D^2}{4} v \tag{13}$$

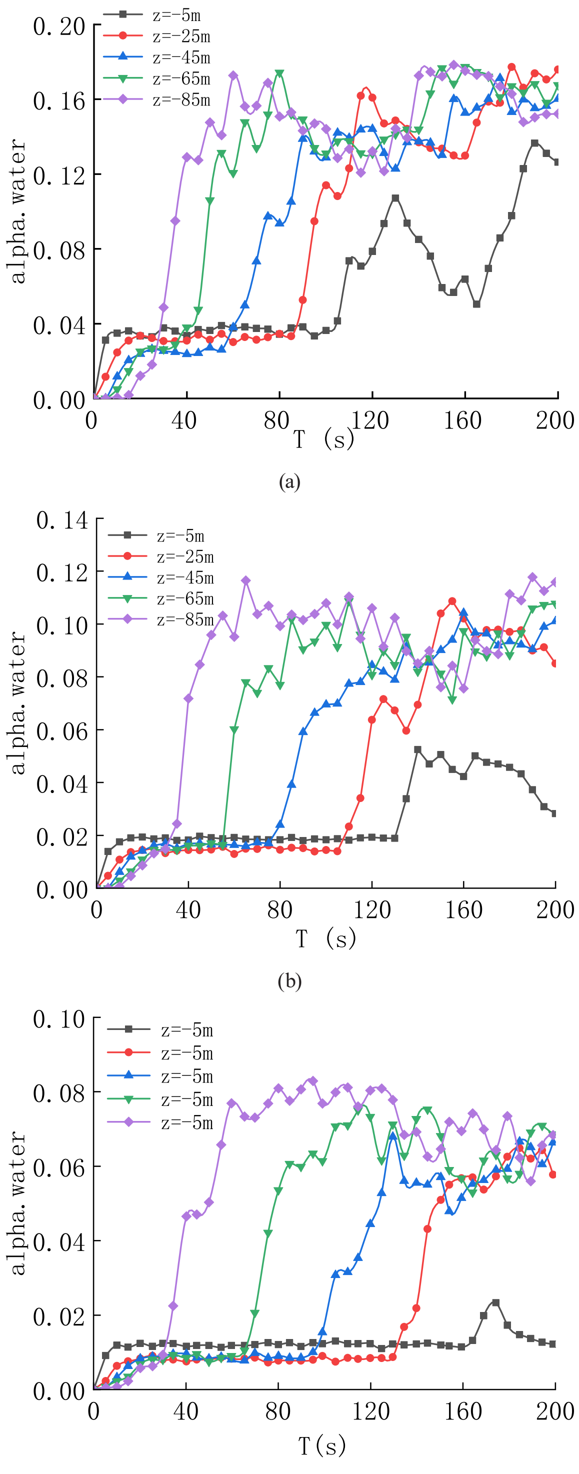

(a)

(b)

(c)

Fig. 10 Monitoring surfaces water level variation trend: (a) D = 2.0 m, (b) D = 1.5 m, (c) D = 1.0 m

3.4 Analysis of the influence of water inlet position on the results

Only the water inlet position is changed, as shown in Table 1, and the trend of water level change on the monitoring surfaces is shown in Fig. 14.

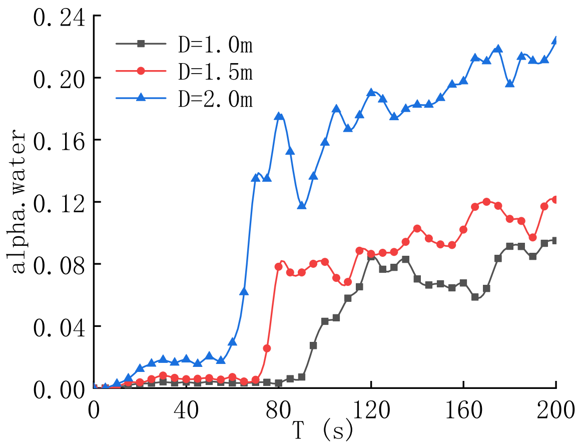

Fig. 11 Cross passage water level variation trend

Fig. 14 shows that by changing the water inlet position, the water level change in the right tunnel is still divided into three stages: the water level rising period, the water level maintaining period, and the water level disorder period. When the water gushes from sidewall, baseplate and vault, the water level of $Z = -5$ m near the tunnel workface continues to rise to a higher level; when the water gushes from baseplate, the water level in the tunnel is the highest and the water inrush velocity is the fastest, followed by sidewall and vault. When the water inrushes from the vault, the water level in the tunnel is the most disordered in the water level disorder period.

The water level change of the cross section of the cross passage at $X = 10$ m is monitored under different water inlet positions. As shown in Fig. 15, the water level increases rapidly after the return water flows into the cross passage. Although the water inflow velocity and inlet diameter are set to be the same, the water inrush occurs in the baseplate, the return water first flows into the cross passage, followed by sidewall and vault.

Analyze the water level in the right tunnel at different water inlet positions when the water inrush does not rush back in a large amount at $t = 20$ s. The water inrush flow pattern is shown in Fig. 16, and the water level comparison is shown in Fig. 17.

Figs. 16 and 17 show that when the water inrush occurs in the baseplate, there is a significant water level difference near the water inrush point, and the water level in the tunnel is the highest, the water level changes most obviously along the tunnel, followed by the sidewall, and the vault is the lowest. Combined with the above analysis, it can be seen that when water inrush occurs at other positions outside the tunnel workface, the lower the water inrush position, the higher the water inrush level in the tunnel, the greater the water level gradient formed, and the water inrush potential energy is converted into kinetic energy, so that the water inrush velocity is greater.

3.5 Analysis of the influence of water outlet conditions on the results

Only the water outlet conditions are changed, as shown in Table 1. The trend of water level change on the monitoring surfaces is shown in Fig. 18.

When the water outlet is set as the entrances of the left tunnel and the right tunnel, the water level in the tunnel rises to a certain level and then floats slightly. Most of the gushing water flows directly out of the tunnel from the entrance of the right tunnel, and there is no stage of sudden increase in water level.

Further analysis of the water level change of the cross section of the cross passage at $X = 10$ m is shown in Fig. 19 (where "*a*" indicates that the water outlet condition is the left tunnel entrance, "*b*" indicates that the water outlet

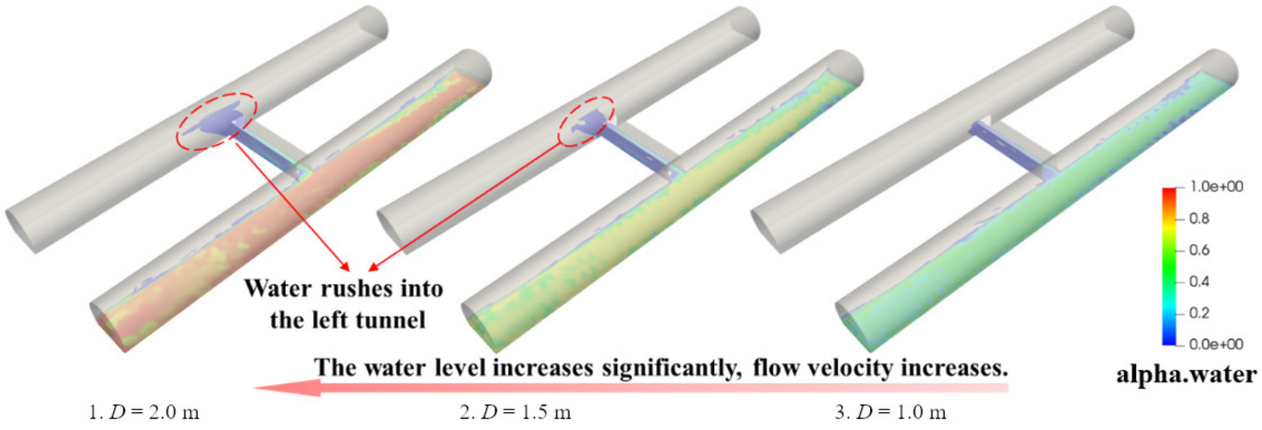

Fig. 12 Water inrush flow pattern

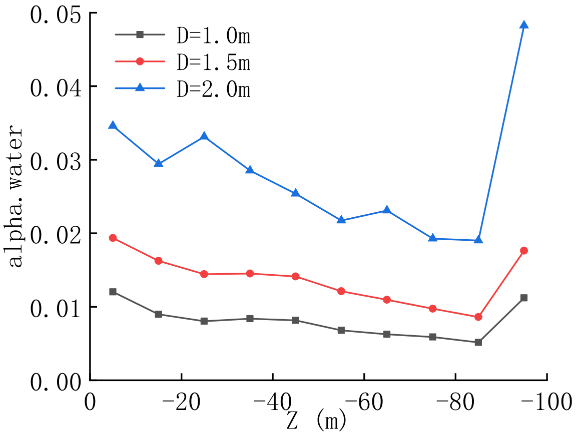

Fig. 13 Comparison of water levels in the right tunnel

condition is the left tunnel and the right tunnel entrances). Before the return water flows into the cross passage, the water levels in the cross passage of situation *a* and situation *b* are similar.

The water level in the right tunnel under different water outlet conditions is analyzed at $t = 20$ s. The water inrush flow pattern is shown in Fig. 20, and the water level comparison is shown in Fig. 21.

Fig. 20 and Fig. 21 show that there is no significant difference in the water level in the tunnel between the two cases before the water rushes back, and the water gushing back is the main reason for the significant difference in the water level between the two situations. Therefore, when the water inrush occurs in situation *b*, evacuating through the right tunnel or utilizing the cross passage to reach the left tunnel exit serves as a viable escape method.

4 Escape route design and suggestions

From the previous analysis of the water inflow process, the escape route when the water inrush occurs in tunnel is preliminarily obtained: pass through the cross passage from the water inrush side and then escape to the tunnel entrance on the other side. In order to further provide the basis for optimizing the escape path, the variation trend of water inrush velocity at different positions in the tunnel is studied. The monitoring lines of water inrush velocity are arranged as shown in Fig. 22 and Table 2.

The typical water inrush conditions in the Section 3 are selected for analysis and research.

4.1 In the case of water inlet $D = 2$ m, $v = 3$ m/s

When a large amount of water flows into the left tunnel, the simulation results are shown in Fig. 23.

From the previous analysis, it can be seen that after the water rushes back, a large amount of water poured into the

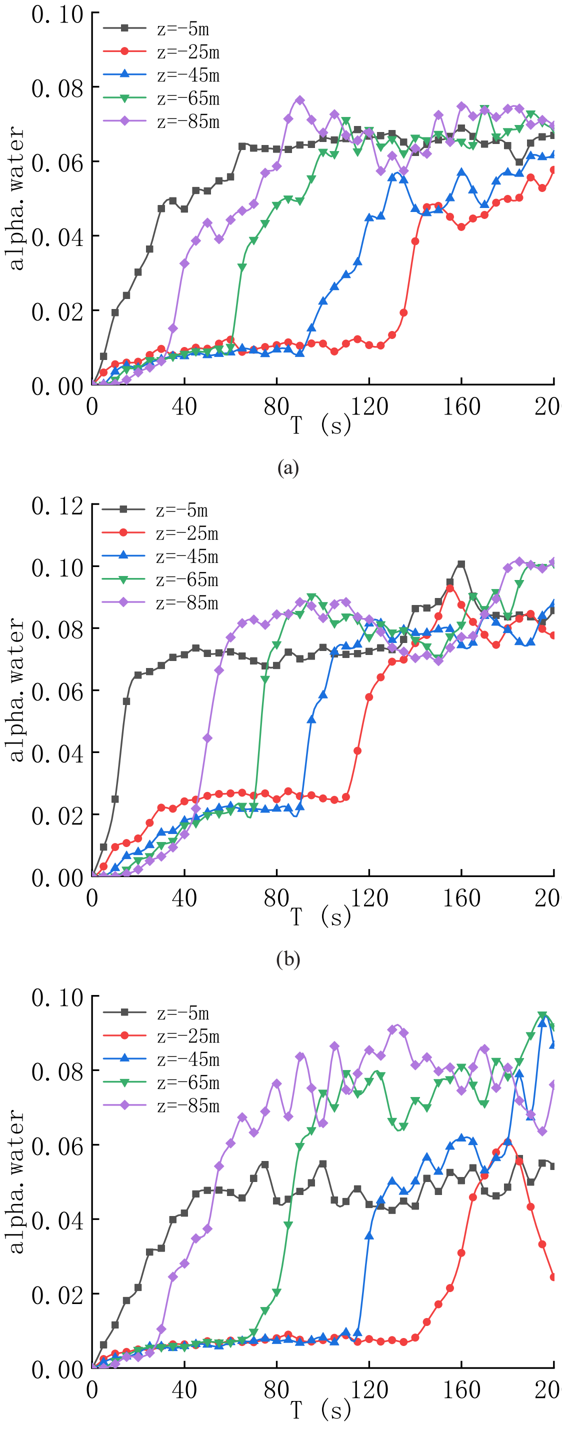

(a)

(b)

(c)

Fig. 14 Monitoring faces water level variation trend: (a) Sidewall, (b) Baseplate, (c) Vault

left tunnel through the cross passage. Fig. 23 (a) shows that when the water gushes into the left tunnel, it showed an obvious "*T*" type flow, and then showed a "*S*" type flow to both ends of the left tunnel, resulting in a particularly chaotic flow, as shown in Fig. 23 (b). In addition, a clear front is formed at the junction of gushing water and returning

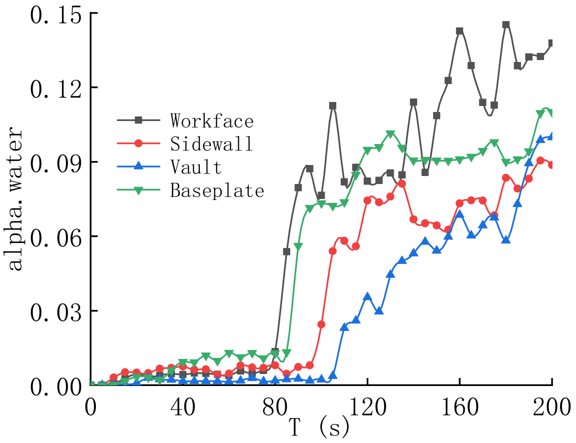

Fig. 15 Cross passage water level variation trend

water, and the water inrush velocity and water level at the front change sharply. The water inrush velocity curves on the monitoring lines in the tunnel are shown in Fig. 24.

Fig. 24 (a) shows that the change trend of water inflow velocity on the monitoring lines $R1$–$R5$ is similar: the water inflow velocity increases rapidly first, then the fluctuation decreases, decreases rapidly at the front and increases between the front and the cross passage. On the monitoring lines $R2$–$R4$, the water inflow velocity has an obvious peak near $Z = -4$ m, and on the $R3$, the flow velocity reaches the maximum of 8.1 m/s. It takes a certain time for the water to flow from the falling point to both sides of the tunnel, and the influence of the water flow velocity on both sides of the tunnel has a lag, reaching a peak of 5.7 m/s near $Z = -10$ m. The water flows from the water inflow point to both sides of the tunnel, and then flows to the middle line of the tunnel after it collides with the sidewall, which explains that $R2$ and $R4$ reach the maximum value of 7.2 m/s near $Z = -20$ m. In general, the water inflow velocity of $R1$ and $R5$ monitoring lines is smaller than that of $R2$–$R4$, and the change trend and velocities are similar. Fig. 24 (b) shows that during the process of water inrush from the right tunnel into the left tunnel through the cross passage, the water inflow velocity has an increasing trend. When it flows into the left tunnel, the

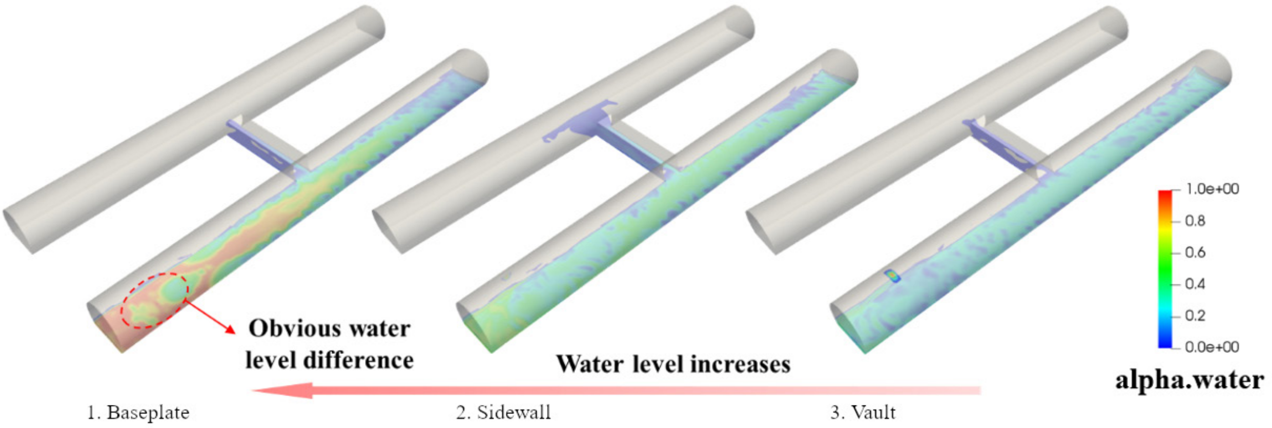

Fig. 16 Water inrush flow pattern

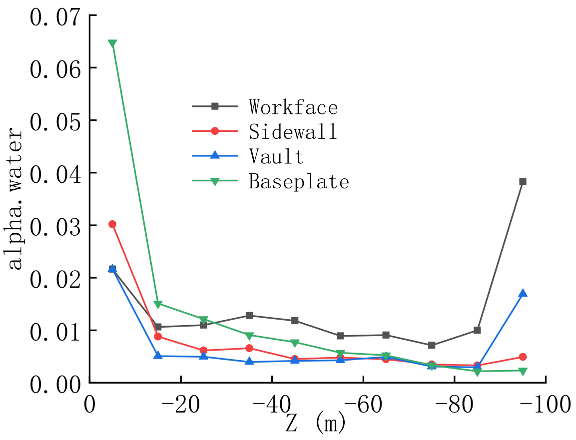

Fig. 17 Comparison of water levels in the right tunnel

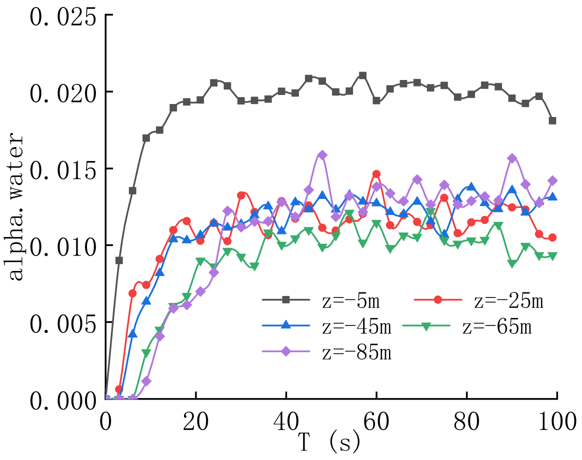

Fig. 18 Monitoring faces water level variation trend

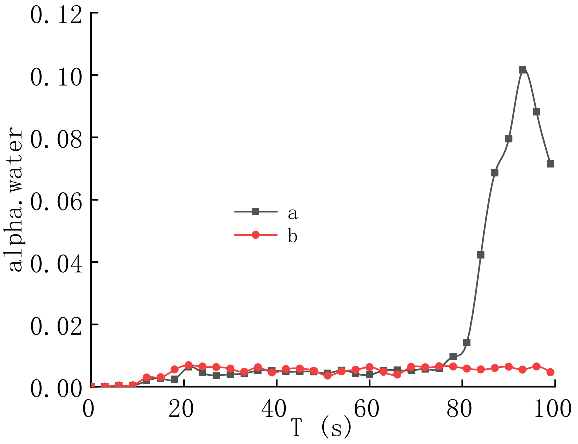

Fig. 19 Cross passage water level variation trend

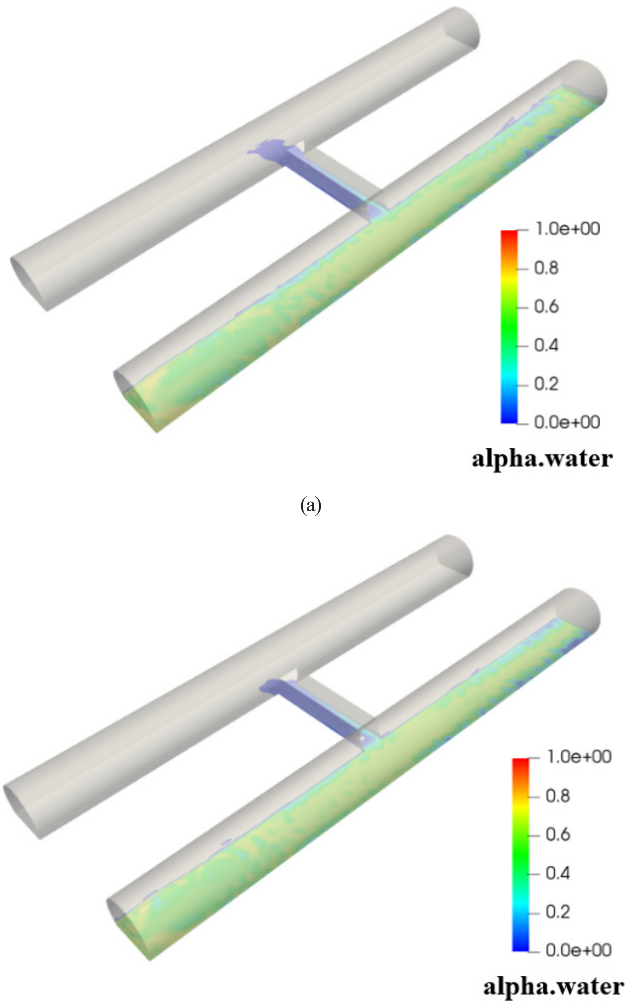

(a)

(b)

Fig. 20 Water inrush flow pattern: (a) Situation *a*, (b) Situation *b*

flow velocity reaches the maximum 4.3 m/s in the center line of the cross passage, and the overall level of water inflow velocity of the *M*1 monitoring line is the smallest. Fig. 24 (c) shows that the gushing water flows disorderly in the left tunnel, but the overall flow velocity is small.

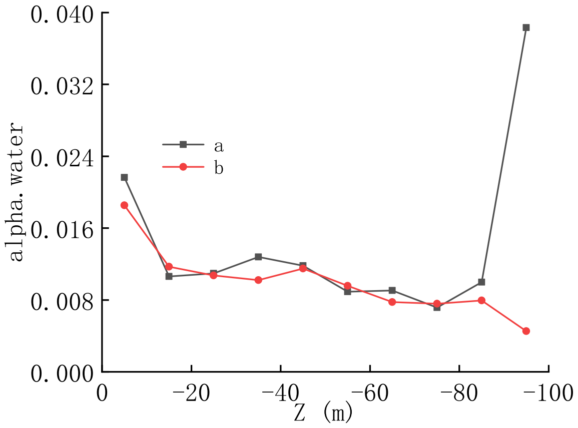

Fig. 21 Comparison of water levels in the right tunnel

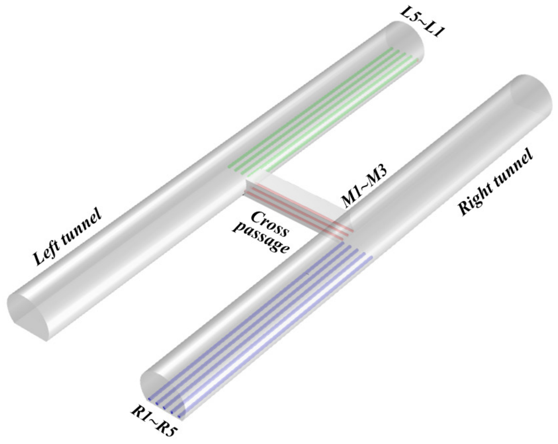

Fig. 22 Velocity monitoring lines layout

Table 2 Monitoring lines information

Monitored location	Monitoring line layout position
Right tunnel	*R*1: $X = 11.5$ m, $Y = 0.1$ m, $Z = 0 \sim -48$ m *R*2: $X = 13.0$ m, $Y = 0.1$ m, $Z = 0 \sim -48$ m *R*3: $X = 15.0$ m, $Y = 0.1$ m, $Z = 0 \sim -48$ m *R*4: $X = 17.0$ m, $Y = 0.1$ m, $Z = 0 \sim -48$ m *R*5: $X = 18.5$ m, $Y = 0.1$ m, $Z = 0 \sim -48$ m
Cross passage	*M*1: $X = 11$ m ~ -11 m, $Y = 0.1$ m, $Z = -48.5$ m *M*2: $X = 11$ m ~ -11 m, $Y = 0.1$ m, $Z = -50.0$ m *M*3: $X = 11$ m ~ -11 m, $Y = 0.1$ m, $Z = -51.5$ m
Left tunnel	*L*1: $X = -11.5$ m, $Y = 0.1$ m, $Z = -52$ m ~ -100 m *L*2: $X = -13.0$ m, $Y = 0.1$ m, $Z = -52$ m ~ -100 m *L*3: $X = -15.0$ m, $Y = 0.1$ m, $Z = -52$ m ~ -100 m *L*4: $X = -17.0$ m, $Y = 0.1$ m, $Z = -52$ m ~ -100 m *L*5: $X = -18.5$ m, $Y = 0.1$ m, $Z = -52$ m ~ -100 m

4.2 In the case of water inlet $D = 1$ m, $v = 5$ m/s

When the gushing water flows into the left tunnel in large quantities, the simulation results are shown in Fig. 25. The change curves of the gushing water velocity of the right tunnel and the cross passage monitoring lines are shown in Fig. 26. The gushing water flows in the left tunnel is disordered and the flow velocity changes irregularly, thus the comparison of the flow velocity of the monitoring lines here is not analyzed.

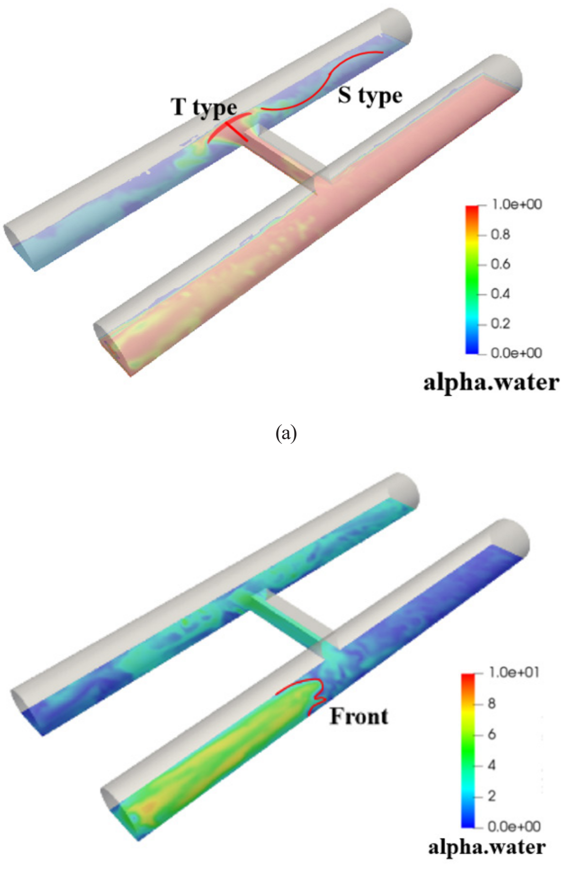

(a)

(b)

Fig. 23 Simulation results: (a) Flow pattern of water inrush, (b) Velocity profile

Water inrush flows to both ends of the left tunnel in a "*T*" shape. Then, the water inrush first collides with the left wall of the left tunnel and flows to the right wall, which makes the water flow in the left tunnel disordered. There is an obvious water inrush levels and water inrush velocity front in the right tunnel near the cross passage, indicating that the water inrush velocity at the higher water level is smaller.

Fig. 26 shows that the water inflow velocity of the monitoring lines *R*1–*R*5 has a similar change trend. The water inflow velocity changes rapidly at both ends of the monitoring lines and maintains a high level between the two ends. The maximum water flow velocity near $Z = -5.5$ m on *R*3 reaches 9.5 m/s, and the water inflow velocity of *R*1 and *R*5 monitoring lines on both sides of the tunnel is smaller than that of *R*2–*R*4. The water inflow velocity in the cross passage increases slowly, reaching a maximum of 4.1 m/s. The overall level of water flow velocity at the monitoring line *M*1 is low, while the water flow velocity at *M*3 is large.

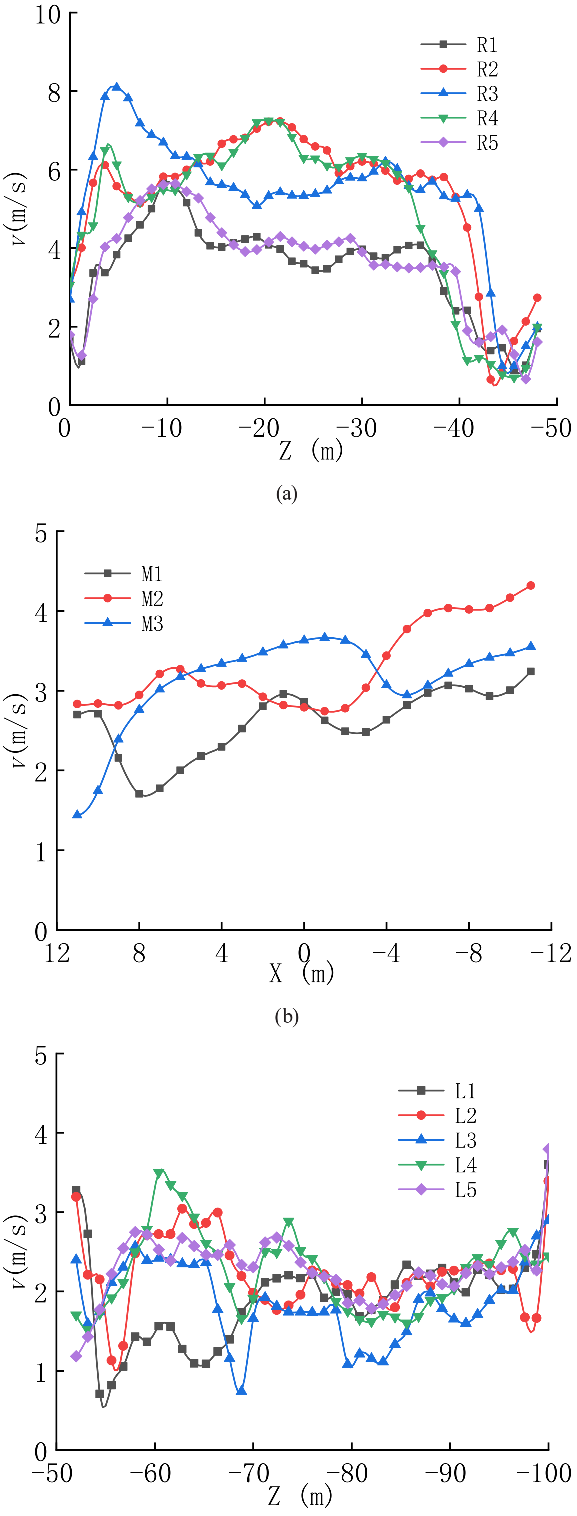

(a)

(b)

(c)

Fig. 24 Velocity curve on monitoring lines: (a) Right tunnel, (b) Cross passage, (c) Left tunnel

4.3 In the case of entrances of left tunnel and right tunnel are water outlet

When more water gushes into the left tunnel, the simulation results are shown in Fig. 27, and the velocity change

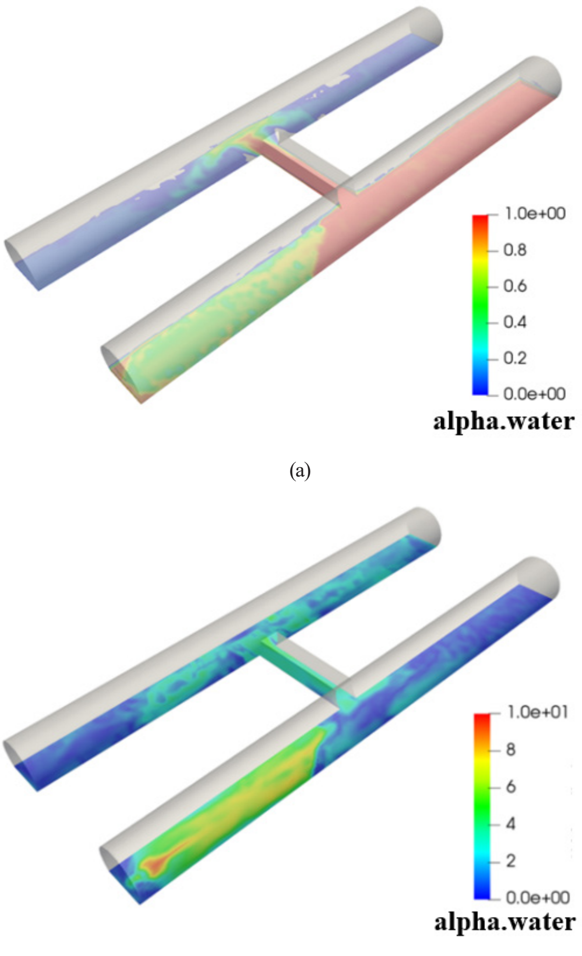

(b)

Fig. 25 Simulation results: (a) Flow pattern of water inrush, (b) Velocity profile

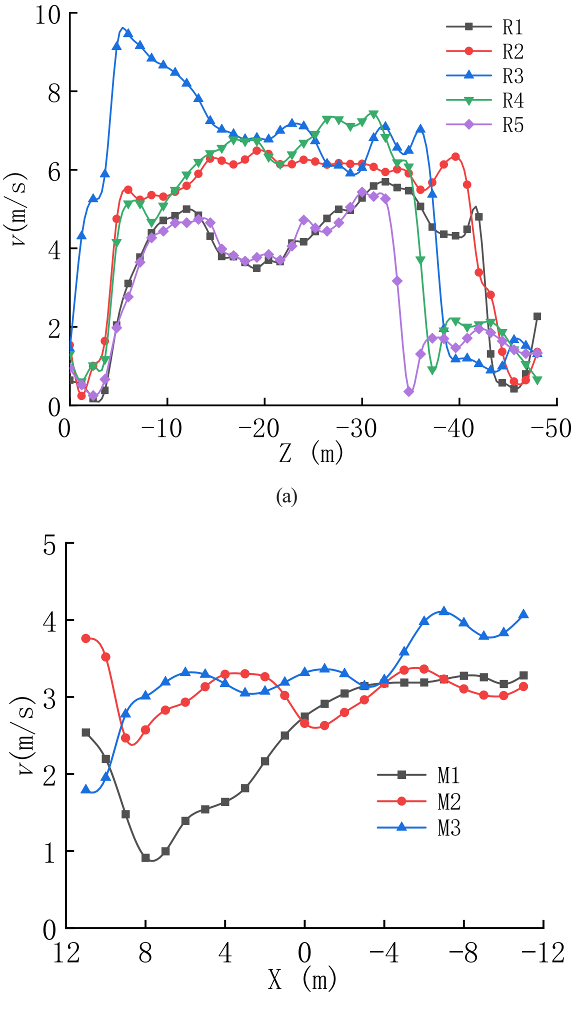

(b)

Fig. 26 Velocity curve on monitoring lines: (a) Right tunnel, (b) Cross passage

curves on the monitoring lines of the right tunnel and the cross passage are shown in Fig. 28.

From the analysis of Section 3, it can be seen that when the left tunnel and the right tunnel entrances are both water outlets, the right tunnel is the dominant channel of water inrush, and a large amount of water gushes directly from the right tunnel entrance. There is no gushing-back water, no water level and velocity front, and the water level of the left tunnel is significantly lower than that of the right tunnel, as shown in Fig. 27.

When the entrances of the left and right tunnels are the water outlets, the right tunnel is the main flow path of the gushing water, so the water flow velocity in the whole right tunnel is analyzed. As shown in Fig. 28 (a), the flow velocity initially rises, peaking at 9.5 m/s at $Z = -8$ m on monitoring line $R3$. Then, the water inflow velocity of monitoring lines $R1$ and $R5$ increases slowly, and the water inflow velocity of monitoring lines $R2$–$R4$ decreases slowly. The flow velocity on both sides of the tunnel near the cross passage exceeds the intermediate flow velocity, indicating that the water inflow velocity on both sides of the tunnel is not necessarily small. The water flow velocity decreases rapidly at the junction of the cross passage and the right tunnel, and then decreases slowly. The water flows more along the sidewall of the cross passage, and the water inflow velocity at the center line is smaller, as shown in Fig. 28 (b).

4.4 In the case of water inrush from baseplate

When a large amount of water flows into the left tunnel, the simulation results are shown in Fig. 29, and the curves of water inflow velocity on the monitoring lines of the right tunnel and the cross passage are shown in Fig. 30.

The gushing water flows into the left tunnel in a "*T*" type and flows to both ends of the left tunnel in a "*S*" type. There is an obvious water level and velocity front at the junction of the gushing water and the returning water.

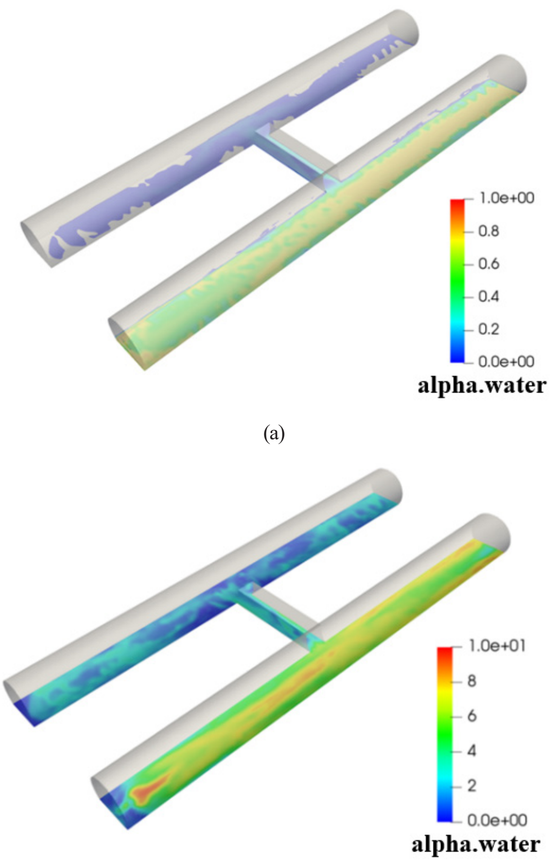

(a)

(b)

Fig. 27 Simulation results: (a) Flow pattern of water inrush, (b) Velocity profile

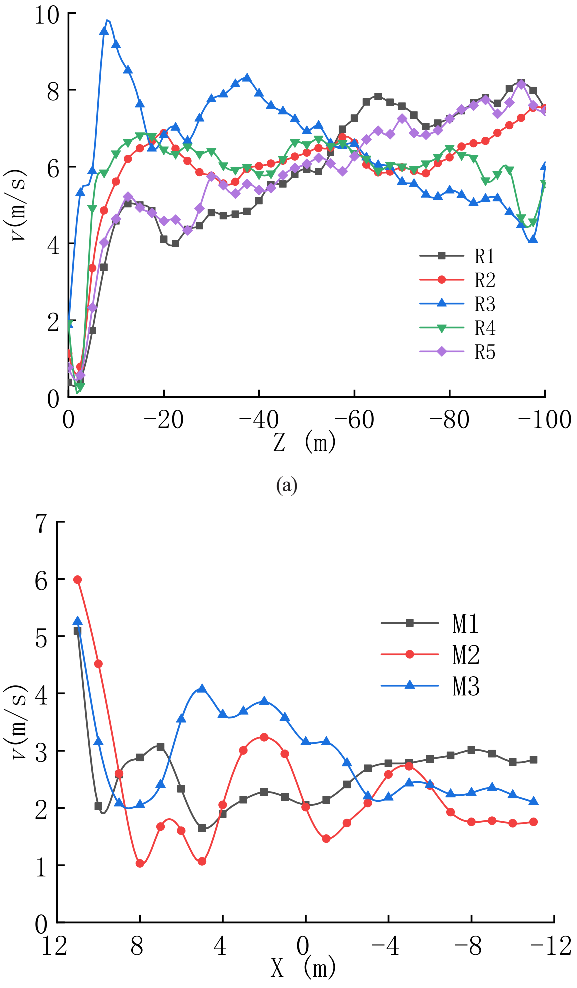

(a)

(b)

Fig. 28 Velocity curve on monitoring lines: (a) Right tunnel, (b) Cross passage

The water level of the gushing point is low and the water flow velocity is fast, as shown in Fig. 29.

It can be seen from Fig. 30 that the overall level of water flow velocity in the right tunnel is low, and the change trend is similar. It increases first, then slows down, and then decreases. The water inflow reaches the maximum velocity of 7.6 m/s near 4 m after the water inrush point. The water inflow velocity is lower on the outer monitoring lines *R*1 and *R*5, and it is greater than the *R*2–*R*4 monitoring lines only at $Z = -20 \sim -28$ m. The water inflow velocity in the cross passage is increasing, and the maximum is 3.4 m/s. The water flow velocity outside the cross passage is small, and *M*1 is the smallest as a whole.

4.5 In the case of water inrush from sidewall

The simulation results of a large amount of water inflow into the left tunnel are shown in Fig. 31, and the curves of water inflow velocity in the right tunnel and the cross passage on the monitoring lines are shown in Fig. 32 respectively.

Due to the constraint of the sidewall of the left tunnel on the water inflow, the water inrush flows into the left tunnel in the form of "*T*" and then flows to both ends of the tunnel in the form of "*S*", which leads to the disorder of the water inflow in the left tunnel. There is an obvious water level and velocity front in the right tunnel, and the area near the water inflow point is the high-velocity area of water inflow, as shown in Fig. 31.

When the water inrush point is on the sidewall, it has a wider impact range. Near $Z = -10$ m, the three monitoring lines *R*2–*R*4 in the middle have a large peak value of water inrush speed, and the water inrush velocity on both sides of the tunnel is low. The water inrush velocity in the cross passage shows a slow increasing trend, and it increases rapidly at $X = 12 \sim 7$ m on *M*3 and $X = -8 \sim -12$ m on *M*1. In general, the water inflow velocity of *M*1 monitoring line is the smallest.

According to the above analysis, when the water inrush occurs in the right tunnel, the water inrush in the first half of the right tunnel has a small flow velocity on both sides of

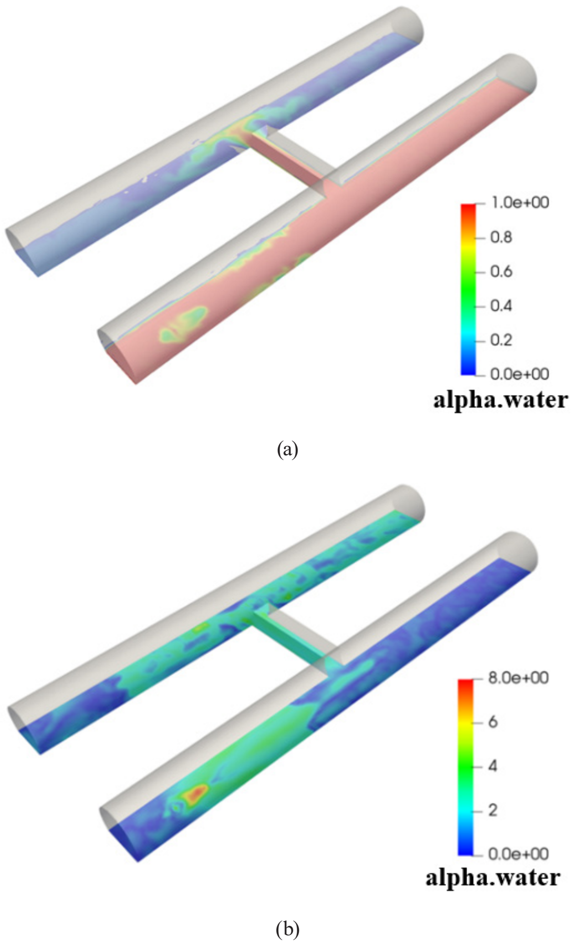

Fig. 29 Simulation results: (a) Flow pattern of water inrush, (b) Velocity profile

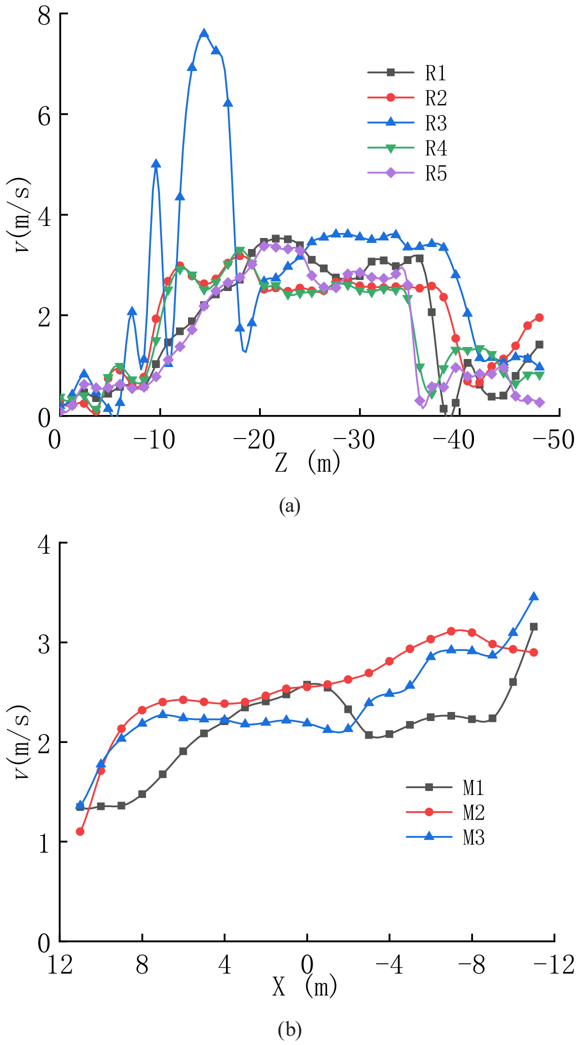

Fig. 30 Velocity curve on monitoring lines: (a) Right tunnel, (b) Cross passage

the tunnel $R1$ and $R5$, and the water inrush velocity on $M1$ in the cross passage is low. The water inrush is "T" type into the left tunnel and flows to both ends of the left tunnel in "S" type. According to the flow pattern of the water inrush in the left tunnel, it can be judged that the right $L1$ of the left tunnel is a feasible escape route. Considering that the rushing-back water in the right tunnel and the tunnel section have influence on escape route, the escape from $R5$ to the cross passage needs to pass through the right tunnel section, which may be in danger through the water inrush, so escape from $R1$ is a better escape route. Thus, when the water inrush occurs in the tunnel, escape from the inside wall of the tunnel with water inrush side, through the inside wall of the cross passage, and finally escape from the inside wall of the tunnel without water inrush side. The escape route is shown in Fig. 33.

5 Conclusions

In order to study the flow characteristics of water inrush in the tunnel and optimize the escape route of water inrush disaster in the tunnel, this paper considers four factors respectively: water inrush velocity, water inlet diameter, water inlet position and water outlet condition. The numerical simulation of water inrush process in tunnel under different water inrush conditions is carried out. According to the numerical simulation results, the distribution of water inrush flow velocity in tunnel is analyzed and studied. The main conclusions are as follows:

The tunnel on the water inrush side is the dominant channel of gushing water flow, and its water level and flow velocity are greater than that of the cross passage; the water level change of the tunnel with water inrush side is divided into three stages: water level rising period, water level maintaining period and water level disorder period.

After the gushing water flows to the tunnel port and rushes back, the water level in the tunnel increases rapidly, forming an obvious flow velocity and water level sudden change front. When the front passes through the

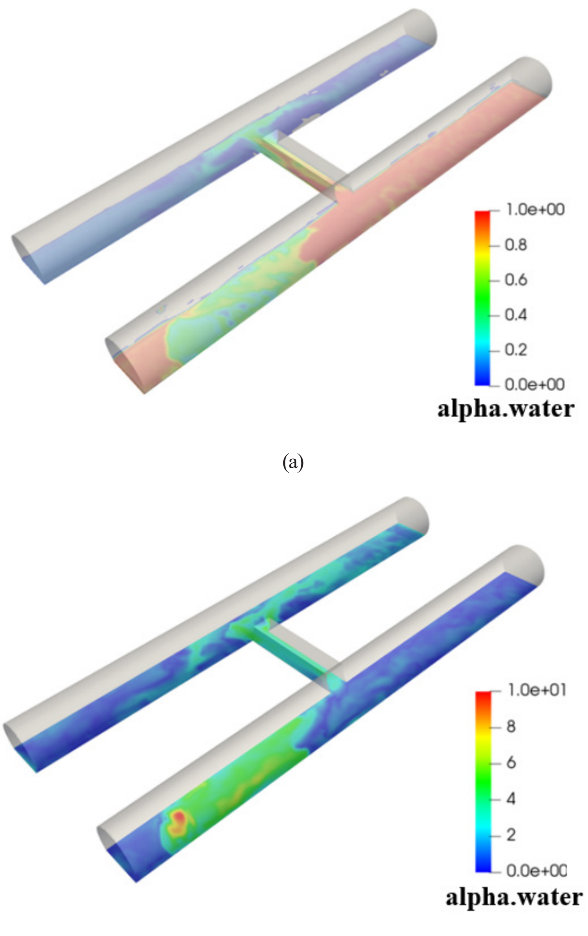

(a)

(b)

Fig. 31 Simulation results: (a) Flow pattern of water inrush, (b) Velocity profile

cross passage, it begins to flood into the tunnel without water inrush side, and the gushing water flow is chaotic. Therefore, it is necessary to avoid the backflow and escape from the cross passage as soon as possible.

When the water inflow velocity or water inlet diameter increases, the increase of water inflow discharge makes the water level and flow velocity in the tunnel increase. When both entrances of the tunnel are water outlets, a large amount of water gushes directly from the tunnel with water inrush side.

When water inrush occurs at other positions, the water inrush from the baseplate forms a higher water level and a faster flow velocity in the tunnel, and the front moves the fastest. Therefore, higher attention should be paid to the water inrush from the baseplate.

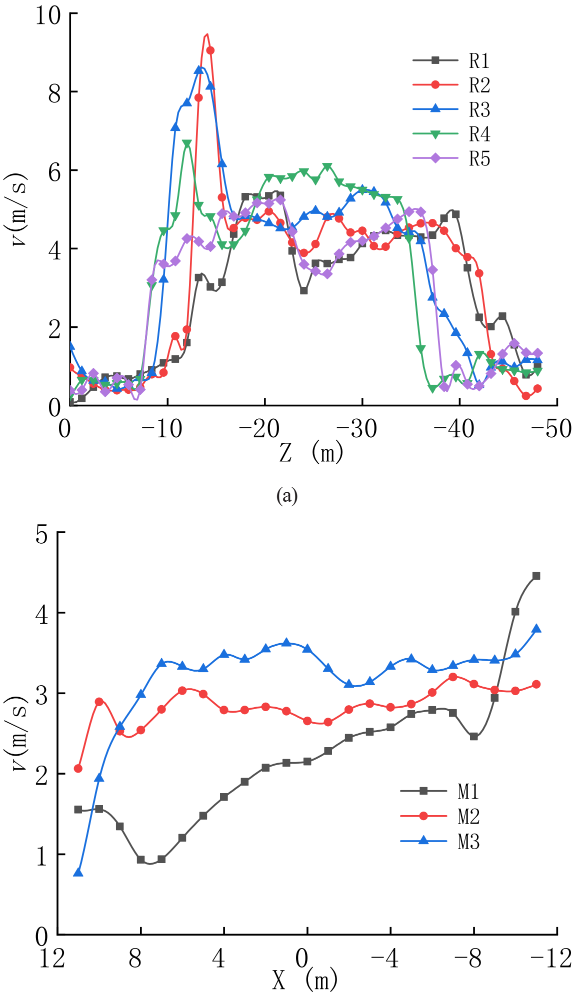

(a)

(b)

Fig. 32 Velocity curve on monitoring lines: (a) Right tunnel, (b) Cross passage

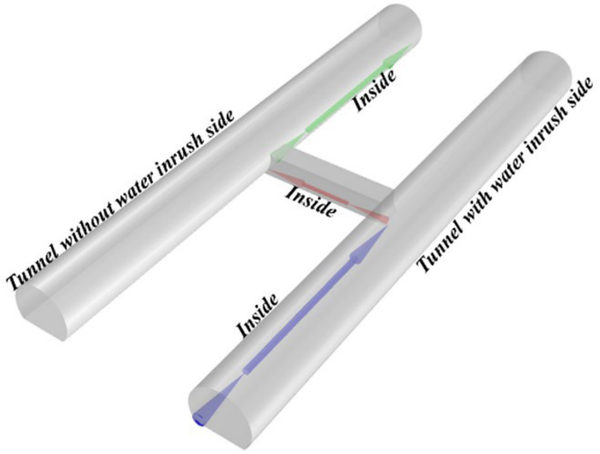

Fig. 33 Escape route

The water flow velocity on both sides of the tunnel with water inrush side is small, and the water inflow velocity through the inside wall of the cross passage is low. The water inflow is "*T*" type into the tunnel without water inrush side, and then flows to both ends of the tunnel in the "*S*" type, the water inflow is disordered, and then the escape route is obtained: from the inside wall of the tunnel with water inrush side, through the inside wall of the cross passage to the tunnel without water inrush side to take refuge, and finally through the inside wall of the tunnel to escape from the tunnel with water inrush disaster.

Acknowledgement

This research was funded by National Natural Science Foundation of China (No. 52279103), the Young Scientists Fund of National Natural Science Foundation of China (No. 52109129), Shandong Provincial Natural Science Foundation (No. ZR2021QE163), the Youth Innovation Team of Shandong Higher Education Institutions (2024KJH100) and Supported by State Key Laboratory for GeoMechanics and Deep Underground Engineering, China University of Mining & Technology (No. SKLGDUEK2113).

References

[1] Li, S., Li, X., Jing, H., Yang, X., Rong, X., Chen, W. "深长隧道突水突泥重大灾害致灾机理及 预测预警与控制理论研究进展" (Research Development of Catastrophe Mechanism and Forecast Controlling Theory of Water Inrush and Mud Gushing in Deep Long Tunnel), China Basic Science, 19(3), pp. 27–43, 2017. (in Chinese)
https://doi.org/10.3969/j.issn.1009-2412.2017.03.005

[2] Qian, Q. "地下工程建设安全面临的挑战与对策" (Challenges faced by underground projects construction safety and countermeasures), Chinese Journal of Rock Mechanics and Engineering, 31(10), pp. 1945–1956, 2012. (in Chienese)
https://doi.org/10.3969/j.issn.1000-6915.2012.10.001

[3] Li, S., Xu, Z., Huang, X., Lin, P., Zhao, X, Zhang, Q., Yang, L., Zhang, X., Sun, H., Pan, D. "隧道突水突泥致灾构造分类、地质判识、孕灾模式与典型案例分析" (Classification, geological identification, hazard mode and typical case studies of hazard-causing structures for water and mud inrush in tunnels), Chinese Journal of Rock Mechanics and Engineering, 37(5), pp. 1041–1069, 2018. (in Chinese)
https://doi.org/10.13722/j.cnki.jrme.2017.1332

[4] Sun, M. "宜万铁路野三关隧道 602 溶腔处治" (602 Karst Cave Treatment in Yesanguan Tunnel on Yichang-Wanzhou Railway), Modern Tunnelling Technology, 47(1), pp. 91–98, 2010. (in Chinese)
https://doi.org/10.13807/j.cnki.mtt.2010.01.010

[5] Lu, J., Liu, X. "玉蒙铁路秀山隧道涌水涌砂地段施工技术" (Construction Techniques for Water and Sand Gushing Section in Xiushan Tunnel on Yuxi-Mengzi Railway), Tunnel Construction, 29(3), pp. 339–341, 2009. (in Chinese)

[6] Yuan, Y., Gao, C., Wang, J., Zhu, Y., Zhang, M. "岩溶隧道突涌水致灾构造与前兆信息判识技术探讨" (Identification of Geological Structures and Precursory Information Likely to Cause Water Inflow in Karst Tunnels), Modern Tunnelling Technology, 55(1), pp. 36–44, 2018. (in Chinese)
https://doi.org/10.13807/j.cnki.mtt.2018.01.005

[7] Li, S., Bu, L., Shi, S., Li, L., Zhou, Z. "Prediction for Water Inrush Disaster Source and CFD-Based Design of Evacuation Routes in Karst Tunnel", International Journal of Geomechanics, 22(5), 05022001, 2022.
https://doi.org/10.1061/(asce)gm.1943-5622.0002305

[8] Li, S., Qi, Y., Li, Z., Zhang, J. "A novel treatment method and construction technology of the pipeline gushing water geohazards in karst region", Tunnelling and Underground Space Technology, 113, 103939, 2021.
https://doi.org/10.1016/j.tust.2021.103939

[9] Li, S., Wang, K., Li, L., Zhou, Z., Shi, S., Liu, S. "岩溶隧道突水灾害形成机理及发展趋势" (Mechanical mechanism and development trend of water-inrush disasters in karst tunnels), Chinese Journal of Theoretical and Applied Mechanics, 49(1), pp. 22–30, 2017. (in Chinese)
https://doi.org/10.6052/0459-1879-16-345

[10] Li, S. C., Zhou, Z. Q., Ye, Z. H., Li, L. P., Zhang, Q. Q., Xu, Z. H. "Comprehensive geophysical prediction and treatment measures of karst caves in deep buried tunnel", Journal of Applied Geophysics, 116, pp. 247–257, 2015.
https://doi.org/10.1016/j.jappgeo.2015.03.019

[11] Wang, M., Yang, W., Zhou, Z., Yang, J., Yang, F., Sheng, S. "Experimental study on fractal characteristics of fault filling medium in the tunnel and relationship between fractal dimension and permeability coefficient", Geomechanics and Geophysics for Geo-Energy and Geo-Resources, 8(1), 6, 2022.
https://doi.org/10.1007/s40948-021-00311-z

[12] Qiao, W., Li, W., Zhang, X., Niu, Y., Chen, Y., Wang, Y., Xing, T. "Prediction of floor water disasters based on fractal analysis of geologic structure and vulnerability index method for deep coal mining in the Yanzhou mining area", Geomatics, Natural Hazards and Risk, 10(1), pp. 1306–1326, 2019.
https://doi.org/10.1080/19475705.2019.1574911

[13] Wu, H., Nian, T., Shan, Z. "Investigation of landslide dam life span using prediction models based on multiple machine learning algorithms", Geomatics, Natural Hazards and Risk, 14(1), 2273213, 2023.
https://doi.org/10.1080/19475705.2023.2273213

[14] Dong, J., Shen, Z., Cao, L., Mi, J., Li, J., Zhao, Y., Mu, H., Liu, L., Dai, C. "Water-sand inrush risk assessment method of sandy dolomite tunnel and its application in the Chenaju tunnel, southwest of China", Geomatics, Natural Hazards and Risk, 14(1), 2196369, 2023.
https://doi.org/10.1080/19475705.2023.2196369

[15] Wu, Y., Ou, X., Wu, B., Jiang, J., Gong, J. "Numerical simulation of water and sediment flow characteristics in tunnels based on Euler-Euler three-phase flow", Physics of Fluids, 36, 023354, 2024.
https://doi.org/10.1063/5.0187683

[16] Li, T., Yang, X. "Risk Assessment Model for Water and Mud Inrush in Deep and Long Tunnels Based on Normal Grey Cloud Clustering Method", KSCE Journal of Civil Engineering, 22(5), pp. 1991–2001, 2018.
https://doi.org/10.1007/s12205-017-0553-6

[17] Pan, D., Zhang, Y., Bu, Z., Xu, Z. "基于层次分析法的岩溶隧道突水突泥风险评估" (Numerical investigation of slurry property effect on grouting and blocking of flowing water in rock fractures), International Journal for Numerical and Analytical Methods in Geomechanics, 47(9), pp. 1681–1698, 2023. (in Chinese) https://doi.org/10.1002/nag.3534

[18] Xu, Z., Li, S., Li, L., Hou, J., Sui, B., Shi, S. "Risk assessment of water or mud inrush of karst tunnels based on analytic hierarchy process", Rock and Soil Mechanics, 32(6), pp. 1757–1766, 2011. https://doi.org/10.3969/j.issn.1000-7598.2011.06.027

[19] Xu, Z., Zhang, Y., Pan, D., Bu, Z. "A Novel Grouting Simulation Method Considering Diffusion and Loss of Slurry in Flowing Water: Interphase Miscible-Transport Time-Tracking (IM-3T) Method", Rock Mechanics and Rock Engineering, 56(8), pp. 5815–5832, 2023. https://doi.org/10.1007/s00603-023-03347-7

[20] He, B. "Numerical Simulation Analysis of Karst Tunnel Water Bursting Movement", In: Proceedings of the 5th International Conference on Civil Engineering and Transportation 2015, Guangzhou, China, 2016, pp. 668–676. ISBN 978-94-6252-134-6 https://doi.org/10.2991/iccet-15.2015.125

[21] Zhou, Y. D., Li, Z. X., Li, C. P., Cao, Z. G. "Design and Realization of Mine Water-Inrush Visualization Simulation System", Advanced Materials Research, 383–390, pp. 6632–6640, 2011. https://doi.org/10.4028/www.scientific.net/AMR.383-390.6632

[22] Zhang, X., Wu, Q., Zhao, Y., Liu, S., Xu, H. "Spatiotemporal modeling of water inrush spreading in mine roadway networks", Water Science and Technology, 85(3), pp. 872–886, 2022. https://doi.org/10.2166/wst.2022.009

[23] Feng, R., Fourtakas, G., Rogers, B. D., Lombardi, D. "A general smoothed particle hydrodynamics (SPH) formulation for coupled liquid flow and solid deformation in porous media", Computer Methods in Applied Mechanics and Engineering, 419, 116581, 2024. https://doi.org/10.1016/j.cma.2023.116581

[24] Feng, R., Fourtakas, G., Rogers, B. D., Lombardi, D. "Two-phase fully-coupled smoothed particle hydrodynamics (SPH) model for unsaturated soils and its application to rainfall-induced slope collapse", Computers and Geotechnics, 151, 104964, 2022. https://doi.org/10.1016/j.compgeo.2022.104964

[25] Holický, M. "Risk analysis and optimization of road tunnels", In: Popov, V., Brebbia, C. A. (eds.) Risk Analysis V: Simulation and Hazard Mitigation, WIT Press, 2006, pp. 57–66. ISBN 978-1-84564-172-6 https://doi.org/10.2495/RISK060061

[26] Yan, G., Feng, D. "Escape-route planning of underground coal mine based on Improved Ant Algorithm", Mathematical Problems in Engineering, 2013(1), 687969, 2013. https://doi.org/10.1155/2013/687969

[27] Ali, M., El-Aziz, A. A., Elwageeh, M. "Optimization of escape routes during mine fire using GIS", Mining Technology: Transactions of the Institutions of Mining and Metallurgy, 132(1), pp. 55–64, 2023. https://doi.org/10.1080/25726668.2022.2163550

[28] Wu, J.., Li, S. C., Xu, Z. H., Huang, X., Xue, Y. G., Wang, Z. C., Li, L. P. "Flow Characteristics and Escape-Route Optimization after Water Inrush in a Backward-Excavated Karst Tunnel", International Journal of Geomechanics, 17(4), 04016096, 2017. https://doi.org/10.1061/(ASCE)GM.1943-5622.0000787

[29] Wu, J., Li, S. C., Xu, Z. H., Pan, D. D., He, S. J. "Flow characteristics after water inrush from the working face in karst tunneling", Geomechanics and Engineering, 14(5), pp. 407–419, 2018. https://doi.org/10.12989/gae.2018.14.5.407

[30] Koshizuka, S. "A particle method for incompressible viscous flow with fluid fragmentation", Computational Fluid Dynamics Journal, 4, pp. 29–46, 1995.